MATTER, MOMENTUM AND ENERGY FLOW IN HEAVY-ION COLLISIONS

M. Prakash[+]
Department of Physics, State University of New York at Stony Brook, Stony Brook, New York 11794, USA

S. Shlomo[++]
Department of Physics and Cyclotron Institute
Texas A&M University, College Station, Texas 77843, USA

B. S. Nilsson and J. P. Bondorf
The Niels Bohr Institute, University of Copenhagen,
DK-2100 Copenhagen Ø, Denmark
and
F. E. Serr[+++]
Center for Theoretical Physics, Laboratory for Nuclear Science,
and Department of Physics, Massachusetts Institute of Technology,
Cambridge, Massachusetts 02139, USA

Abstract

We study the flow of matter, momentum and energy in low energy heavy-ion collisions. This is done by using the Wigner phase space distribution function to calculate quantum mechanical analogs of the classical distributions of the observables. We apply the Wigner transformation to time dependent Hartree-Fock calculations of $^{16}O + ^{16}O$ and $^{40}Ca + ^{40}Ca$ reactions. Both static and dynamic features of the distribution functions are demonstrated.

1. Introduction

There now exist many studies of both static and dynamic properties of nuclei using the Wigner distribution function (WDF)[1-8]. Our aim here is to obtain new insights into the dynamics of heavy-ion collisions through the WDF. Rather than evolving the WDF itself, we construct it from wave functions resulting from a dynamical theory. For this we use the time dependent Hartree-Fock (TDHF) approximation[9]. We summarise results of calculations for head-on collisions of $^{16}O + ^{16}O$ and $^{40}Ca + ^{40}Ca$ reactions. TDHF studies of these reactions have been done before using other methods[9].

2. The Wigner Distribution Function

The Wigner phase space distribution function $f(\vec{r},\vec{k},t)$, is given by the shifted Fourier transform of the one-body density matrix $\rho(\vec{r},\vec{r}',t)$;

$$f(\vec{r},\vec{k},t) = (1/2\pi)^3 \int d\vec{s}\, e^{-i\vec{k}\cdot\vec{s}}\, \rho(\vec{r}+\vec{s}/2, \vec{r}-\vec{s}/2, t) \qquad (2.1)$$

In the present work, we consider $\rho(\vec{r},\vec{r}',t)$ obtained in the TDHF approximation. In this case,

$$\rho(\vec{r},\vec{r}',t) = \sum_j n_j\, \phi_j^*(\vec{r},t)\, \phi_j(\vec{r}',t) \qquad (2.2)$$

where n_j are the occupation numbers, and $\phi_j(\vec{r},t)$ are the single particle wave functions calculated from the TDHF mean field. Since we deal with head-on collisions of heavy-ions, we make use of the axial symmetry and write the single particle wave functions in the form

$$\phi_j(\vec{r},t) = \phi_j(\vec{r}_\perp, z, t)\, e^{i m_j \Phi} \qquad (2.3)$$

where $\vec{r}_\perp$ is the position vector perpendicular to z, Φ is the azimuthal angle, and m_j is the angular momentum projection on z. Physical observables are obtained by evaluating integrals of the form $\langle O\rangle = \int f(\vec{r},\vec{k})\, O(\vec{r},\vec{k})\, d\vec{r}\, d\vec{k}$. Therefore, of special interest are projections $\tilde{f}$, in which some of the arguments are integrated out. We consider a few such projections in the following.

(i) $$\tilde{f}(z, k_z, t) = \int d^2\vec{r}_\perp\, d^2\vec{k}_\perp\, f(\vec{r}_\perp, z, \vec{k}_\perp, k_z, t) \qquad (2.4)$$

(ii) $$\tilde{f}(z, \vec{k}_\perp, k_z, t) = \int d^2\vec{r}_\perp\, f(\vec{r}_\perp, z, \vec{k}_\perp, k_z, t) \qquad (2.5)$$

These projected distribution functions are predominantly positive. We will also consider the WDF along the symmetry axis of the system, viz.,

$$f(\vec{r}_\perp = 0, z, \vec{k}_\perp, k_z, t) \qquad (2.7)$$

The Static WDF

A knowledge of the static WDF is very useful for understanding the dynamic WDF. The static HF wave functions $\phi_j(r)$ in eq. (2.2)

were calculated using an effective interaction consisting of the direct Coulomb interaction and modified Skyrme force II, with no spin orbit interactions. The details of the numerical calculation of the WDF are described in ref. 10. The HF results can be compared with those for Fermi gas (FG) and Harmonic oscillator (HO) models for which analytical results can be derived. For the infinite Fermi gas, we have $f^{FG}(\vec{r},\vec{k}) = 4/(2\pi)^3\ \theta(k_F^2 - k^2)$ where k_F is the Fermi momentum. For finite nulei, the WDF oscillates around f^{FG}, due to the presence of shell and surface effects[3,12]. This is illustrated clearly by the exact expression for the WDF for nucleons in closed shells of a spherically symmetric HO potential[8], viz.

$$f^{HO}(\vec{r},\vec{k}) = f^{HO}(\varepsilon) = (4/\pi^3)\sum_k n_k (-1)^k e^{-\varepsilon} L_k^2(2\varepsilon) \qquad (2.8)$$

where $L_K^{\alpha}(x)$ is the associated Laguerre polynomial and $\varepsilon = k^2/\nu + \nu r^2$, with $\nu = m\omega/\hbar$. The factor 4 takes into account spin-isospin degeneracy. The expressions of eq. (2.8) are

$$\begin{aligned} f^{HO}(\varepsilon) &= (8/\pi^3)\, e^{-\varepsilon}(\varepsilon - 1) \qquad \text{for } A = 16 \\ f^{HO}(\varepsilon) &= (8/\pi^3)\, e^{-\varepsilon}(\varepsilon-1)(\varepsilon-2) \qquad \text{for } A = 40 \end{aligned} \qquad (2.9)$$

We see that for finite nuclei, the WDF acquires negative values in specific regions of the phase space, and unlike f^{FG}, extends beyond the Fermi momentum, k_F. For open shell nuclei in the HO model, the WDF is more complicated than eq. (2.8) in that it depends on the angle between $\vec{r}$ and $\vec{k}$[8]. The WDF for any numerical single particle wave function can be calculated by expanding it in a HO basis and using eq. (28) of ref. 8.

The solid lines of fig. 1 show the projected WDF $\tilde{f}(z,k_z)$, for the HF wave functions, at the center and near the surface. The corresponding results shown for the Fermi gas model are obtained by integrating $f^{FG}(\vec{r},\vec{k})$ to give $\tilde{f}^{FG}(z,k_z)=(1/2\pi)(R^2-z^2)(k_F^2-k_z^2)$. We have determined the equivalent sharp surface radius, R, from the relation $R^2=(5/3)\langle r^2\rangle_{HF}$, and $k_F=(9\pi A/8)^{1/3}/R$, from the particle number normalization. We also show in fig. 1 the projected WDF for the harmonic oscillator, $\tilde{f}^{HO}(z,k_z)$, which is obtained from eq. (2.9). The size parameters $\nu = m\omega/\hbar$ were determined by using the root mean square radii of the HF calculations. We see in fig. 1 that the FG model roughly matches the magnitude of $\tilde{f}^{HF}(z,k_z)$ at z = 0

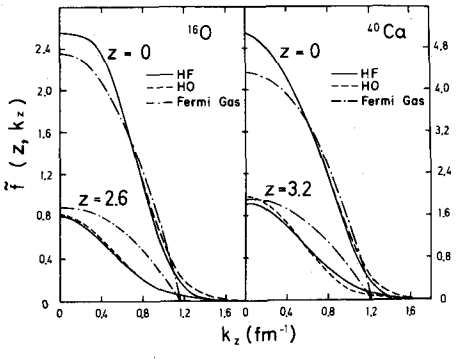

Fig. 1. Projected Wigner distribution functions (eq.(2.4)) for static nuclei at the center and near the nuclear radius.

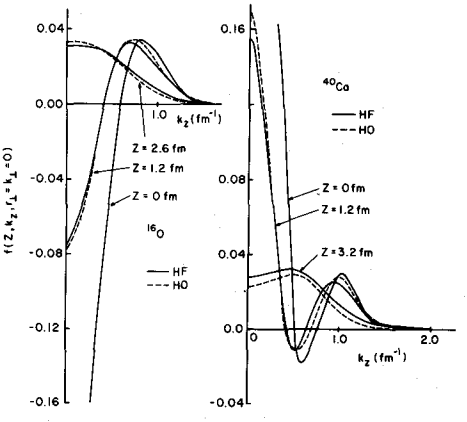

Fig. 2. Cross-sectional cuts for the WDF (eq.(2.7)) for static nuclei at different distances.

and for small k_z, but cannot give the high momentum tail of the distribution. Understandably, the agreement between the two models is worst in the surface of the nucleus. The HO results more accurately reproduce the HF calculations. There is an excess of high momentum components in $\tilde{f}^{HO}(z,k_z)$ at z = 0, and of lower k_z in the nuclear surface.

We notice that $f^{HO}(\vec{r},\vec{k})$ given in eq. (2.9) has negative values for certain values of $\vec{r}$ and $\vec{k}$. This feature also appears in the HF calculations. In fig. 2, we plot $f(z,k_z,\vec{r}_\perp = \vec{k}_\perp = 0)$, obtained from eq. (2.7) for different values of z, along with the corresponding HO results. The HO model reproduces the HF results very well. In the surface, however, the HF calculations predict more high momentum components than the HO model. In both models, the WDF is positive in the surface.

The Dynamic WDF

Using TDHF wave functions, we have calculated the WDFs given in eqs. (2.4), (2.5) and (2.7). The effective Hamiltonian in the TDHF calculations was the same as that used in the static HF calculations.

The contours of the projected WDF, $\tilde{f}(z,k_z,t)$, in fig. 3 show the space momentum correlation during the course of the $^{40}Ca+^{40}Ca$ reaction at E/A = 5.0 MeV. At t = 0, the shift along the k_z axis is equal to $k_{rel} = 0.94\ fm^{-1}$. For $0.20\times10^{-21}sec < t < 0.4\times10^{-21}sec$, the distribution function is that of a dinuclear complex. During this time there is a spilling over of nucleons from one ion to the other. This can most easily be seen by following the maximum $\tilde{f}(z,k_z,t)$ contour as a function of time. Beyond $t = 0.4 \times 10^{-21}$ sec, rapid changes of the WDF in the neck region are observed. For $t>0.6\times10^{-21}$ sec, the centers of the two distributions are well separated along the z axis. The shift along the k_z axis is now smaller than at t = 0, which shows that energy loss in relative motion has taken place.

In fig. (4) we show the cross-sectional cuts, $f(z,k_z,\vec{r}_\perp=\vec{k}_\perp=0)$ at three representative values of z, for the $^{16}O + ^{16}O$ reaction at E/A = 1.25 MeV and the $^{40}Ca + ^{40}Ca$ reaction at E/A = 5.0 MeV, respectively. Note that, for the symmetric A reactions we consider, $f(-\vec{r},\vec{k}) = f(\vec{r},-\vec{k})$. The time in both figures has been chosen such that the two nuclei overlap considerably with each other. The figures show that the dynamic WDF also has large negative values. As in the static case, the WDF is positive in the surface of the dinuclear complex.

In both figs. 3 and 4, we see that the WDF vanishes for $\vec{r}=\vec{k}=0$. This follows from the idempotent condition for $f(\vec{r},\vec{k})$ and the prevailing symmetry. Given that the density matrix comes from a Slater determinant, we have[9a]

$$f(\vec{r},\vec{k}) = (2\pi)^3 e^{-i/2\left(\nabla_r^{(1)}\cdot\nabla_k^{(2)} - \nabla_r^{(2)}\cdot\nabla_k^{(1)}\right)} f^{(1)}(\vec{r},\vec{k})\, f^{(2)}(\vec{r},\vec{k}) \qquad (2.10)$$

where the superscripts (1) and (2) indicate which WDF's the derivatives act upon. Taking the real and imaginary parts (remember f is real):

$$f(\vec{r},\vec{k}) = (2\pi)^3 \cos\left[\tfrac{1}{2}\left(\nabla_r^{(1)}\cdot\nabla_k^{(2)} - \nabla_r^{(2)}\cdot\nabla_k^{(1)}\right]\right] f^{(1)}(\vec{r},\vec{k})\, f^{(2)}(\vec{r},\vec{k})$$

$$0 = (2\pi)^3 \sin\left[\tfrac{1}{2}\left(\nabla_r^{(1)}\cdot\nabla_k^{(2)} - \nabla_r^{(2)}\cdot\nabla_k^{(1)}\right]\right] f^{(1)}(\vec{r},\vec{k})\, f^{(2)}(\vec{r},\vec{k}) \qquad (2.11)$$

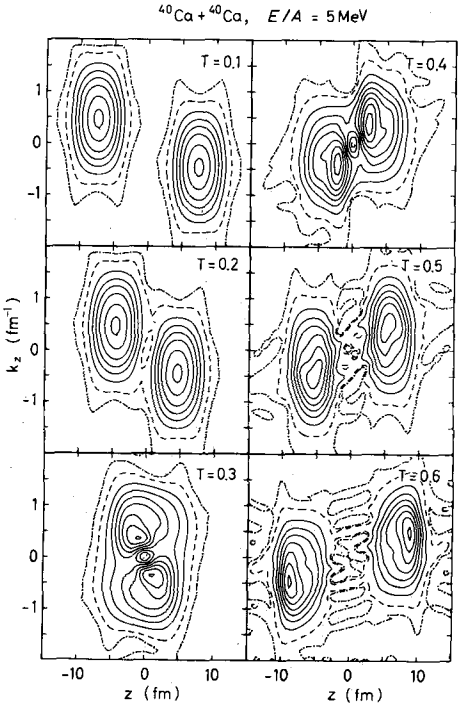

Fig. 3.

The projected WDF $\tilde{f}(z,k_z,t)$ (eq. (2.5)). Time is in units of 10^{-21} sec. The dash-dot and dashed contours correspond to f=0.02 and 0.2 respectively. For t=0.3, 0.4 and 0.6, the seven solid contours are associated with f=0.8(0.8)5.6 starting from the outermost one. For other times, we show six solid contours with f=0.8(0.8)4.8. Note that for all times, $\tilde{f}(z=k_z=0)=0$.

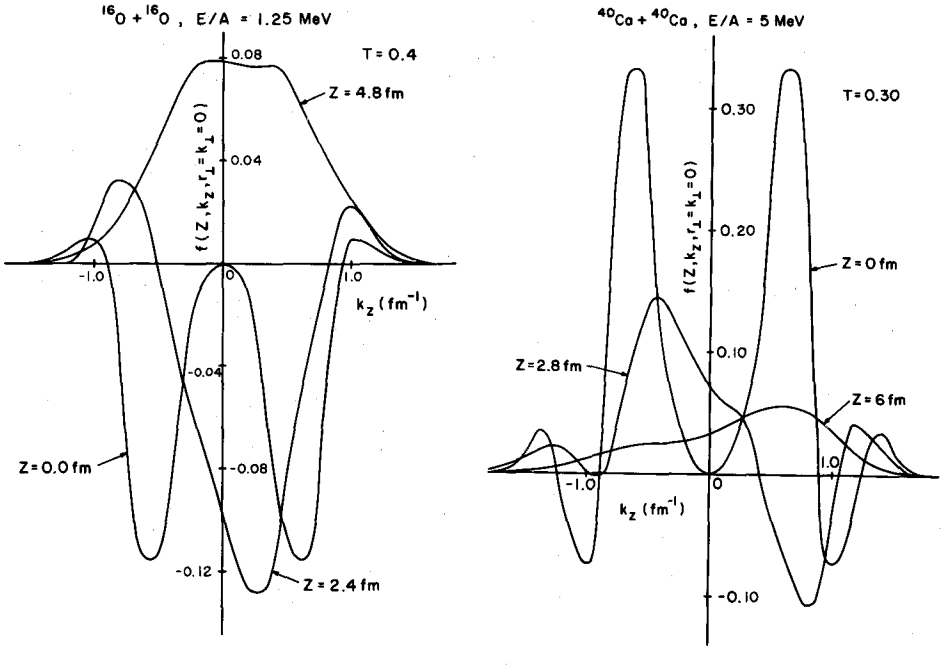

Fig. 4. Cross-sectional cuts of the WDF during the dynamics. Time is in units of 10^{-21} sec.

While the second condition is trivially satisfied, the first condition is nontrivial, since it contains terms like $(\nabla_r f^{(1)} \nabla_k f^{(2)})^2 - (\nabla_r f^{(1)} \nabla_r f^{(2)})(\nabla_k f^{(1)} \nabla_k f^{(2)})$ which in general do not vanish. Now for collisions between identical nuclei, in the c.m. system (not necessarily head on) the symmetry $f(\vec{r},-\vec{k}) = f(-\vec{r},\vec{k})$ implies that $[\nabla_r f]_{\vec{k}=\vec{r}=0} = [\nabla_k f]_{\vec{r}=\vec{k}=0} = 0$. At the origin, then, the Slater determinant condition becomes $f(0,0) = (2\pi)^3 [f(0,0)]^2$ independent of time. This requires $f(0,0) = 0$ or $1/(2\pi)^3$. Since $f(0,0,t=0) = 0$, it will stay that way.

3. Momentum and Energy Flow

In this section, we investigate the flow of momentum during the reaction. In fig. 5 we show the quantity

$$\tilde{f}(k_z, k_\perp, t) = \int_{z\geq 0} \tilde{f}(z, k_z, \vec{k}_\perp, t)\, dz \qquad (3.1)$$

for the $^{16}O+^{16}O$ reaction at E/A = 1.25 MeV and the $^{40}Ca+^{40}Ca$ reaction at E/A = 5 MeV. Eq. (3.1) gives the momentum distribution in the positive half of z space only. Therefore, at the lowest value of t we have a smooth distribution corresponding to the ground state momentum distribution of one nucleus centered around $k_z=(1/2)k_{rel}$. The plateau in the region $|\vec{k}-(1/2)\vec{k}_{rel}| \sim 0.6$ fm^{-1} in fig. 5(b) is due to shell structure. During the interaction time, momentum components associated with nucleons transferred from the other nucleus, as well as components associated with collective excitations are present in the z>0 space. These are clearly seen by the peaks and shoulders of the curves in fig. 5. The distribution for the largest t still differs considerably from a totally thermalized distribution. The absence of two-body collisions in the TDHF approximation naturally leads to very slow thermalization of the separated fragments.

The flow of momentum and energy in the perpendicular direction might have important consequences on the dynamics. To quantify this aspect of heavy-ion collision dynamics, we investigate the behaviour of the parallel and perpendicular components of the total kinetic energy during the reaction. In terms of the WDF, the total kinetic energy T is defined by

$$T = \int \tau_W(\vec{r})\, d\vec{r} = \int (\hbar^2 k^2/2m) f(\vec{r},\vec{k},t)\, d\vec{r}\, d\vec{k} \qquad (3.2)$$

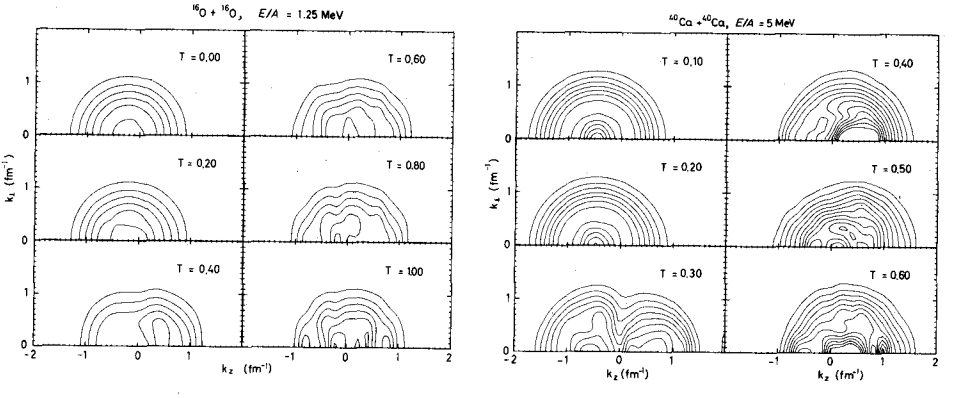

Fig. 5. The momentum distribution in the z>0 space (eq. (3.1), as a function of the parallel and perpendicular components of momentum. Time is in units of 10^{-21} sec. Starting from the outermost one, the contours are associated with $\tilde{f}$ = 0.4(0.4)2.4 in fig.(a). Contours in fig.(b) are associated with $\tilde{f}$ = 1.0(1.0)12.0.

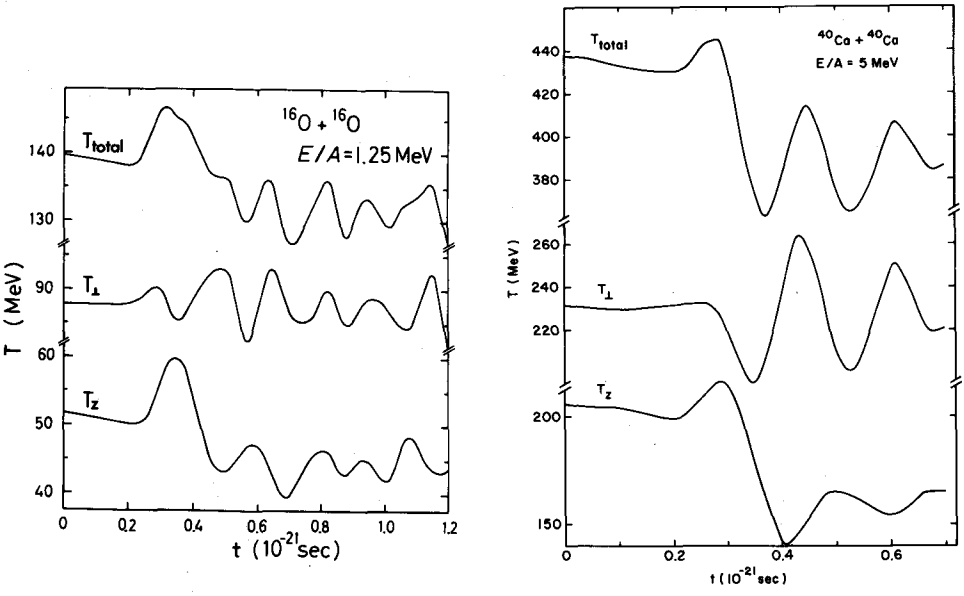

Fig. 6. The kinetic energy as a function of time. T_z and $T_\perp$ are the components of kinetic energy parallel and perpendicular to the reaction axis z ($T = T_z + T_\perp$).

We separate the parallel and perpendicular components of T, denoted T_z and $T_\perp$, by replacing k^2 by k_z^2 or $k_\perp^2$ in eq. (3.2). In fig. 6, we show T_z, $T_\perp$ and T during the $^{16}O + ^{16}O$ reaction at E/A = 1.25 MeV, and $^{40}Ca + ^{40}Ca$ reaction at E/A = 5.0 MeV, respectively. At t = 0, $T_z = (1/2)T_\perp + T_{rel} - V_c$, where T_{rel} is the initial kinetic energy with which the ions are boosted towards each other, and V_c is the Coulomb interaction energy at the initial separation. As the two nuclei overlap, T_z, $T_\perp$ and T begin to oscillate. The change in $T_\perp$ during the interaction time is comparable to that for T_z. In the exit channel, T_z and $T_\perp$ oscillate out of phase. These results imply that there is a considerable redistribution of energy between the parallel and perpendicular components of kinetic energy during the reaction. In so far as the outcome of the TDHF dynamics is dependent on what happens during the interaction time, allowing dynamics to take plae only in a plane and freezing the wave functions in the third direction could lead to significantly different results.

4. Matter flow

The exchange of nucleons between the colliding ions is studied by using the concept of a one-way current defined in terms of the WDF[11]. A semi-classical interpretation is given to the one-way current, which allows for a comparison with static approaches. In terms of the WDF, the current density $\vec{j}(\vec{r},t)$ is given by

$$\vec{j}(\vec{r},t) = \int (\hbar\vec{k}/m)\, f(\vec{r},\vec{k},t)\, d\vec{k} \qquad (4.1)$$

The one-way current density in the direction of a unit vector $\hat{z}$ is defined as

$$j_+(\vec{r},t) = \int_{k_z\geq 0} d\vec{k}\ (\hbar k_z/m)\, f(\vec{r},\vec{k},t) \qquad (4.2)$$

From eq. (4.2), one has that $j = j_+ + j_-$. In the Fermi gas model, $j_+ = \hbar k_F^4/8\pi^2 m)$, which is the bulk flux in nuclear matter. Closed expressions have also been derived for j_+ in the HO model[10,12]. Integrating eq. (4.2) over the perpendicular components of space the one-way current $\Phi_+(z,t)$ across a plane at z is given by

$$\Phi_+(z,t) = \int_0^\infty (\hbar k_z/m)\, \tilde{f}(z,k_z,t)\, dk_z \qquad (4.3)$$

In the dynamic situation, our interest is in the flow of nucleons between the two ions. For a reaction between nuclei of identical masses this is given by the one-way current of particles

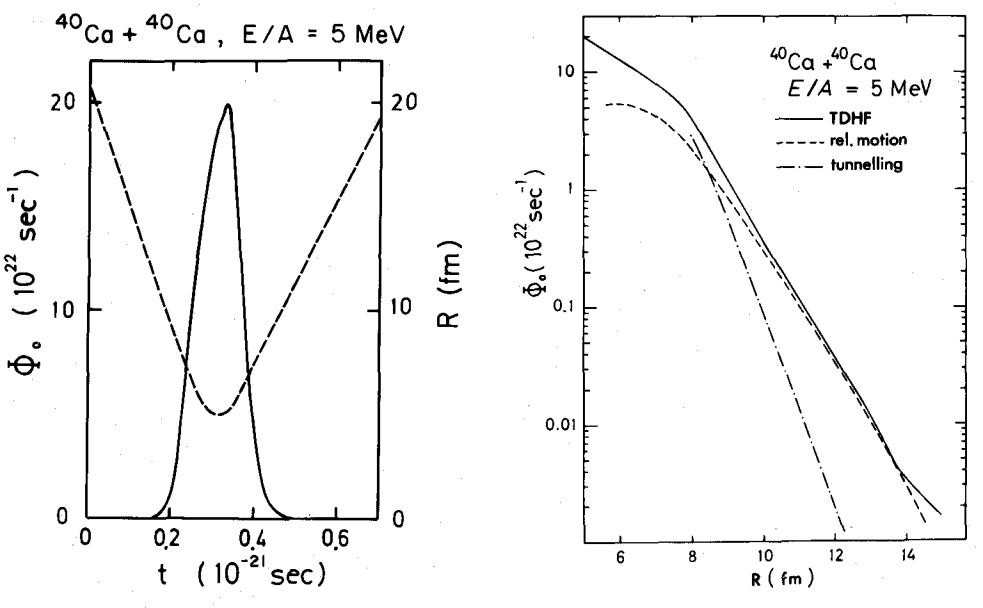

Fig. 7. (a). The solid curve shows the TDHF one-way current across the z = 0 plane dividing the two colliding nuclei as a function of time. The dashed curve shows the fragment separation R (scale on right).
(b). Currents as a function of the fragment separation R. The models are explained in the text.

$\Phi_0 = \Phi_+(z=0,t)$ across the plane z = 0 dividing the two ions. Since Φ_0^{TDHF} is found to be practically unchanged when averaged over a length $\sim k_F^{-1}$, we expect it to give a good description of the one-way current in a semi-classical sense. In fig. 7, we show Φ_0^{TDHF} (solid line) vs.t, and the fragment mass separation coordinate R(t), for the ^{40}Ca + ^{40}Ca reaction at E/A = 5.0 MeV.

We can understand the TDHF one-way current in terms of some simpler models. For example, for large separations we expect the flux to come primarily from the tails of wave functions being carried along by the relative motion of the two self-consistent potential wells. This flux due to relative motion must be extracted before comparing the TDHF results with static models[13,14] for the tunnelling through and over the potential barrier. Also, static models can only give the one-way current as a function of the distance between the ions. We therefore compute Φ_0^{TDHF} vs.R during the approach phase of the reaction, shown by the solid curve of fig. 7, for the ^{40}Ca reaction at E/A = 5.0 MeV. We concentrate on the approach phase

because the simple models we now consider for the contributions from relative motion and nucleon tunnelling do not explicitly include deformation of the ions. Deformation effects should be smaller during the approach phase than during the exit phase.

First, we study the contributions from relative motion alone. Motivated by the expected large-distance behaviour, we move the frozen initial HF density profile of one of the ions past the z = 0 plane, with a time dependent average relative velocity determined from the TDHF calculations. The dashed curve in fig. 7 shows $\Phi_0^{\text{rel.motion}}$ for the ^{40}Ca reaction at E/A = 5.0 MeV. For distances much larger than the contact distance of the spherical initial half-potential radii R_c = 8 fm, the contribution from relative motion within the frozen density approximation accounts for most of the one-way current Φ_0^{TDHF}. However, when the densities of the two ions begin to overlap considerably, $\Phi_0^{\text{rel.motion}}$ falls below Φ_0^{TDHF}. At the minimum values of R, dR/dt, and hence $\Phi_0^{\text{rel.motion}}$, will fall to zero.

In the second step, we study the one-way current due to nucleon tunnelling through and over the potential barrier, ignoring relative motion. We use a model based on the approach of Ko et al.[14]. It is important that our static calcculations mimic the details of the forces in the TDHF calculations as closely as possible. We have therefore used the potential along the z-axis resulting from the TDHF calculations to determine the transmission probability. The results for the ^{40}Ca reaction are shown by the dash-dotted curve in fig. 7. Near the contact distance R_c, $\Phi_0^{\text{tunnelling}}$ is comparable to $\Phi_0^{\text{rel.motion}}$. However, for $R > R_c + 2$ fm, the one-way current due to tunnelling is extremely small.

Comparing the combination of the one-way currents due to relative motion and tunnelling to the TDHF results, we find that, at distances large compared to the contact distance R_c, Φ_0^{TDHF} is almost entirely due to the relative motion. Near R_c, the sum of the contributions from relative motion and tunnelling is close to the calculated TDHF one-way current. The comparison is not as meaningful for very compact configurations because some of our approximations are no longer valid. Better agreement should be obtained by refining the models for the two contributions.

Integrated One-Way Currents

We denote by N_{ex} the time integrated one-way current across the z = 0 plane and list it in table 1. Roughly speaking, N_{ex} may classically be taken to represent the total number of particles exchanged from one side to the other during the course of the reaction. In order to understand the qualitative behaviour of N_{ex}^{TDHF}, we consider two nuclei in free motion boosted towards each other by a momentum $(1/2)k_{rel}$. When there is no interaction and no antisymmetrization between the two nuclei we have,

$$N_{ex}^{\text{Free motion}} = A + (4/k_{rel}) \int_{(1/2)k_{rel}}^{\infty} (k_z - (1/2)k_{rel}) \hat{f}(k_z)\, dk_z \qquad (4.10)$$

where A is the number of particles in one of the nuclei. With the projected momentum distributions from the static HF configurations as inputs, the calculated results are shown in table 1. $N_{ex}^{\text{Free motion}}$ saturates at A for large k_{rel}. This kinetic effect may also be seen in the TDHF results. However, the simple free motion model overestimates N_{ex}. Considerable reduction may be expected from the Pauli exclusion principle. Estimates from the free Fermi gas model which are based on the plane wave Born approximation (PWBA) predict too large reduction factors for the low enrgy reactions. Results for finite nuclei calculated using the HO model and the PWBA are not very different from the FG predictions. Table 1 summarises these findings. More realistic estimates for finite nuclei which are based on the DWBA approximation[15] are expected to yield better agreement with the TDHF results.

Table 1.

Reaction	$(E/A)_{CM}$ (MeV)	N_{ex}^{TDHF}	$N_{ex}^{\text{Free motion}}$	N_{ex} Pauli blocking F.G. model	N_{ex} Pauli blocking H.O. model
$^{16}O+^{16}O$	1.25	15.1	35.81	9.74	8.95
	5.00	10.5	18.85	10.5	13.76
	10.0	10.2	16.68	12.73	15.68
$^{40}Ca+^{40}Ca$	5.00	15.9	47.83	26.64	38.5

5. Outlook

We have seen that with the help of the WDF, it is possible to study several aspects of the heavy-ion collision dynamics. Its application is by no means restricted to the TDHF approximation we have chosen to illustrate the course of dynamics. While in principle it provides no more information than obtained from wave functions, the WDF sometimes provides a convenient way of calculating quantities which have a classical or semi-classical analog, emphasizing at the same time the essential differences in the quantum world[7]. Other applications of such calculations would be to determine the momentum region of cluster formation and prompt particle emission in heavy-ion collisions.

+ Supported by the U.S. Department of Energy under contract DE-AC02-76ER with the State University of New York.

++ Supported by the National Science Foundation under contract PHY-8109019.

+++ Supported by the U.S. Department of Energy under contract DE-AC02-76ER03069, and the National Science Foundation under contract PHY-7801164.

References

1. E. P. Wigner, Phys. Rev. 40 (1932) 749;
2. G. F. Bertsch, Nucl. Phys. A249 (1975) 253; Many Body Dynamics of Heavy-Ion Collisions, in: Les Houches Lecture Notes, ed. R. Balian et al., (North-Holland, Amsterdam, 1978), pp. 178-262.
3. N. L. Balazs and G. G. Zipfel, Jr., Ann. Phys. 77 (1973) 139; N. L. Balazs and H. C. Pauli, Z. Phys. A281 (1977) 395; A277 (1976) 265.
4. P. Ring and P. Schuck, The Many-Body Problem (Springer-Verlag, New York, 1980) Chap. 13, and references therein.
4a. V. M. Kolomietz and H. H. K. Tang, Physica Scripta 24 (1981) 915.
4b. D. M. Brink and M. D. Toro, Nucl. Phys. A372 (1980) 151.
4c. C. Y. Wong, Phys. Rev. C25 (1982)1460.
5. J Richert et al., Phys. Lett. 87B (1979); Nucl. Phys. A356 (1981) 260.
6. H. S. Köhler and H. Flocard, Nucl. Phys. A323 (1979) 189; H. S. Köhler, Nucl. Phys. A343 (1980) 315.
7. H. H. K. Tang, et al., Phys. Lett. 101B (1981) 10.
8. S. Shlomo and M. Prakash, Nucl. Phys. A357 (1981) 157.
8a. J. Hüfner and M. C. Nemes, Phys. Rev. C23 (1981)2538.
9. S. E. Koonin, in Progress in Particle and Nuclear Physics, Vol.4, edited by D. Wilkinson (Pergamon, Oxford, 1980) pp. 283.
9a. S. E. Koonin, Ph.D. Thesis, 1975, Massachusetts Institute of Technology (unpublished).
10. M. Prakash et al., Nucl. Phys. A (in print).
11. M. Prakash, Phys. Rev. Lett. 47 (1981) 898.
12. M. Prakash et al., Nucl. Phys. A370 (1981) 898.
13. J. Randrup, Nucl. Phys. A307 (1978) 319, and Ann. Phys. 112 (1978) 356.
14. C. M. Ko, Phys. Lett. 77B (1978) 174.
15. S. Shlomo and P. J. Siemens, to be published; G. Bertsch and O. Scholten, MSU preprint 1981.